ACS NANO

www.acsnano.org

ARTICLE

Elastic Instability of Cubic Blue Phase Nano Crystals in Curved Shells

Sepideh Norouzi, Antonio Tavera-Vazquez, Johanan Ramirez-de Arellano, Dae Seok Kim, Teresa Lopez-Leon, Juan J. de Pablo,* Jose A. Martinez-Gonzalez,* and Monirosadat Sadati*

Cite This: *ACS Nano* 2022, 16, 15894–15906

Read Online

ACCESS | Metrics & More | Article Recommendations | Supporting Information

ABSTRACT: **Many crystallization processes, including biomineralization and ice-freezing, occur in small and curved volumes, where surface curvature can strain the crystal, leading to unusual configurations and defect formation. The role of curvature on crystallization, however, remains poorly understood. Here, we study the crystallization of blue phase (BP) liquid crystals under curved confinement, which provides insights into the mechanism by which BPs reconfigure their three-dimensional lattice structure to adapt to curvature. BPs are a three-dimensional assembly of high-chirality liquid crystal molecules arranged into body-centered (BPI) or simple cubic (BPII) symmetries. BPs with submicrometer cubic-crystalline lattices exhibit tunable Bragg reflection and submillisecond response time to external stimuli such as an electric field, making them attractive for advanced photonic materials. In this work, we have systematically studied BPs confined in spherical shells with well-defined curvature and boundary conditions. The optical behavior of shells has also been examined at room temperature, where the cholesteric structure forms. In the cholesteric phase, perpendicular anchoring generates focal conic domains on the shell's surface, which transition into stripe patterns as the degree of curvature increases. Our results demonstrate that both higher degrees of curvature and strong spatial confinement destabilize BPI and reconfigure that phase to adopt the structure and optical features of BPII. We also show that the coupling of curvature and confinement nucleates skyrmions at greater thickness than those observed for a flat geometry. These findings are particularly important for integrating BPs into miniaturized and curved/flexible devices, including flexible displays, wearable sensors, and smart fabrics.**

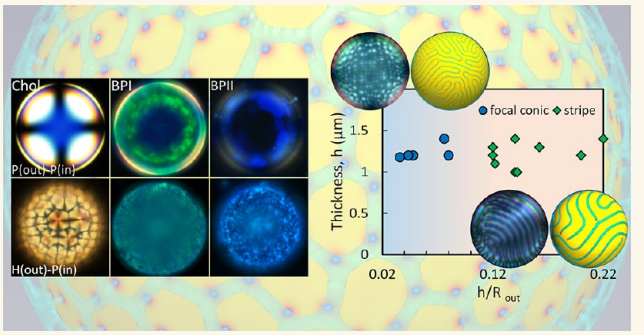

KEYWORDS: *blue phase, liquid crystals, skyrmions, curved confinement, elastic instability*

INTRODUCTION

Curved crystalline arrangements are ubiquitous in nature, for example, in insect eyes, radiolaria, biomineralization, and ice nucleation. They have attracted interest due to the fundamental and technological relevance of the interplay between curvature, structure, and functionality.[1,2] Stress-induced by the curvature of 3D space can frustrate crystal lattice formation, influence growth pathways, and modify equilibrium states by forming topological defects.[3−5]

In this work, we integrate experimental measurements and theoretical simulations to unveil the mechanism by which blue phase (BP) soft crystals nucleate and grow when they are confined in geometries of varying Gaussian curvature. BPs are frustrated mesophases that appear at a temperature between cholesteric and isotropic phases in high-chirality liquid crystals, where the chiral pitch length, p is only a few hundred nanometers. The pitch length, the parameter to measure the strength of the chirality = $2\pi/p$, is defined as the distance required for the local nematic director, $\boldsymbol{n}$ to complete a full 2π rotation. At a sufficiently high-chirality or small pitch length (p < 500 nm), liquid crystal molecules organize into double-twisted cylinders (DTC), which subsequently self-assemble to form a three-dimensional cubic lattice structure. These biaxially oriented DTCs are stabilized by line defects (disclination lines),[6−11] whose orientation determines two crystal packing structures named BPI, with body-centered cubic lattice symmetry, and BPII, with simple cubic lattice symmetry.[12,13] BPs with submicrometer crystal lattice parameters give rise to selective Bragg reflection of visible light. Moreover, the liquid nature of these soft crystals enables

Received: March 21, 2022
Accepted: September 20, 2022
Published: September 27, 2022

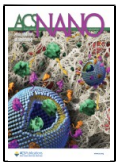

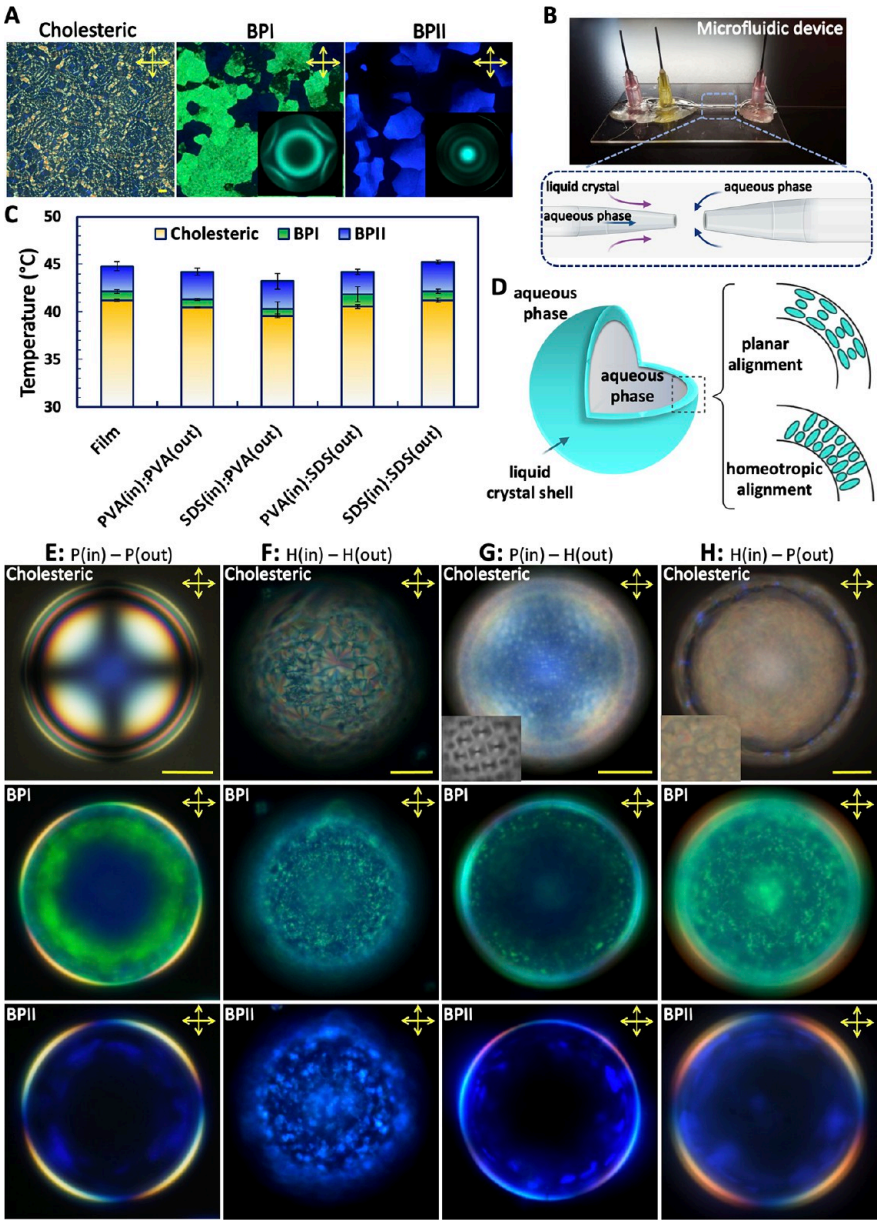

Figure 1. Configurational order and optical appearance of cholesteric and BP shells for various boundary conditions. (A) Cholesteric phase, BPI and BPII in a 12 μm thick film and their corresponding Kossel diagrams (inset), (B) microfluidic device, (C) transition temperature of high-chirality liquid crystal in film (bulk state) compared to shells with various boundary conditions, (D) schematic of chiral molecular ordering in core−shells with planar and homeotropic surface anchoring conditions, reflection-mode cross-polarized images of cholesteric and BPs confined in shells with (E) degenerate planar anchoring at inner and outer interfaces (P(in)−P(out)), (F) homeotropic anchoring at inner and outer interfaces (H(in)−H(out)), (G) degenerate planar anchoring inside and homeotropic anchoring outside (P(in)−H(out)), (H) homeotropic anchoring inside and degenerate planar anchoring outside (H(in)−P(out)) (scale bar = 20 μm).

submillisecond switching times and tunable photonic band gap properties, making them ideal candidates for application in soft photonic materials, where their solid counterparts cannot be employed. In addition, the structures tuned by external stimuli prefigure applications from optoelectronics, photonics, and actuators to chemo/biosensors.[14−16] BP soft mesoscopic crystals can easily adjust to geometrical constraints; the distortion induced in the underlying molecular order can trigger the formation of distinct configurations, as well as peculiar phase behaviors that could shift or expand the stability range of BPs. Although past work has shown the behavior of BPs in confined geometries can be markedly different from that in bulk, important questions remain to be addressed.

Fueled by the technological demand for miniaturized devices, confined BPs in the submicrometer scale have been the subject of recent computational, theoretical, and experimental studies. Some of the key variables that have been found to influence conformational behavior and defect formation in BPs are physical confinement, surface anchoring, and anchoring strength.[17−27] Theoretical studies by Fukuda and co-workers have demonstrated that confining a high-chirality liquid crystal with a small pitch length in a nanoscale gap between two flat surfaces can lead to the formation of distinct arrays of disclination lines, including double helices, winding lines, and staggered structures of disclinations as well as skyrmions and half-skyrmions, controlled by the degree of

https://doi.org/10.1021/acsnano.2c02799
ACS Nano 2022, 16, 15894−15906

confinement and surface anchoring.[28−31] Skyrmions are localized particle-like topological defects with constant order parameter magnitude in an orientational order parameter field that cannot anneal away. In a full skyrmion, the director field in a chiral liquid crystal, $\boldsymbol{n}$ makes a full π rotation as it moves from the skyrmion center to the periphery. In a half-skyrmion, on the other hand, the director field rotates radially by $\frac{\pi}{2}$ from the skyrmion center outward.[30,31]

Spatial curvature in constrained environments, such as droplets, spheroids, and shells, can host even more intricate chiral assemblies due to the coupling of curvature and various boundary conditions. The effect of curvature and surface anchoring on the configuration of chiral droplets and shells has been studied in the low-chirality limit (p > 500 nm), where the system transitions from cholesteric structure to isotropic phase without forming BPs. It has been found that tuning the droplet size and p in droplets with weak planar surface anchoring stabilizes a single helix or a double twisted structure.[32] Altering p in droplets with strong degenerate planar anchoring, alternatively, can reconfigure the chiral droplets from a twisted bipolar structure to a radial spherical arrangement.[33] Upon transition from degenerate planar to homeotropic anchoring, on the other hand, chiral droplets undergo a substantial rearrangement forming structures reminiscent of 2D skyrmions.[34] Spherical shell as a versatile platform has also been used to study the interplay of bulk elasticity, confinement, and surface anchoring in low-chirality liquid crystals. A radial spherical structure composed of two braided defect lines has been observed in planar-aligned chiral shells, which transform to stripe patterns and focal conic domains upon transition to homeotropic orientation.[35,36] In Janus cholesteric shells, low-chirality liquid crystals form both cholesteric fingers and skyrmions, which can transition between various types by tuning the boundary conditions and applying external stimuli.[37] The rich dynamic spatial patterns observed in the cholesteric phase of the chiral shells can be further developed to engineer colloidal assemblies or chiro-optic devices.[38−40]

In the case of high-chirality BPs (p < 500 nm), past numerical and computational studies have found major structural changes in the underlying cubic lattice structures upon confinement in curved geometries. In particular, computational studies have predicted arrays of defect lines and hexagonal patterns in BPs confined into submicrometric scale droplets.[41] They have further illustrated the higher stability of BPs in curved geometries with weak planar anchoring relative to the bulk. Simulations by Palacio-Betancur *et al.*[42] have delineated the rich configurational behavior of high-chirality liquid crystals in spheroidal geometries, both as a function of anchoring strength and aspect ratio. They have shown that the inhomogeneous topological curvature of a spheroid directs the structural reorganization of defect lines into regions of high curvature and, for moderate surface anchoring, additional BP-like and hybridized BP morphologies can emerge. In the same line of study, the experimental and computational simulations of BPs confined in extended prolate domains have revealed the emergence of two distinct BP regions with different transition temperature characteristics.[43]

The effect of geometrical confinement and curvature on the BP structures are limited to a few theoretical and experimental studies, where high-chirality BPs are confined in droplets or spheroid.[20,41−43] To the best of our knowledge, there are no systematic experimental or numerical studies of high-chirality liquid crystals and their underlying 3D lattice structures when confined in shells with double-curved boundaries. The geometrical incompatibility between the 3D cubic lattice structures of BPs and curvature can significantly constrain the organization of these nanostructures within curved, miniaturized spaces. In what follows, we investigate the structure of high-chirality liquid crystals in the cholesteric phase and when they form BPs as a function of shell thickness, curvature, and surface anchoring conditions. We begin by presenting their optical properties, phase behavior, and configurational order as a function of surface anchoring conditions. We then examine the effect of shell thickness and curvature on the configurational order of the cholesteric and BP shells. Our experimental observations are accompanied by computational simulations that provide detailed insights into the underlying physics of the molecular rearrangements and the corresponding optical features observed in experiments.

RESULTS AND DISCUSSION

The high-chirality liquid crystal with $p \approx 260$ nm was prepared by doping a chiral molecule (S-811) in a benzotriazole-based nematic liquid crystal (MLC-2142) at a concentration of 37 wt %, where BPs can form. Subsequently, the optical properties and phase behavior of the mixture were examined in a sandwich geometry between two cover glasses with degenerate planar anchoring separated with 12 μm thick spacers. The reflection mode polarized optical micrographs of the mixture reveal the formation of the cholesteric structure at room temperature, which transitions to BPI and subsequently to BPII at 40.5 and 41.5 °C, respectively (Figure 1A,C). The BPI and BPII structures were verified by distinct reflectance peaks at 530 and 450 nm, respectively (Supporting Information (SI), Figure S1), which can be associated with the Bragg diffraction from [110] and [100] planes of the conoscopy interference patterns (insets in Figure 1A).[44] To investigate the effect of double-curved confinement on the spatial arrangement and phase behavior of the high-chirality cholesteric structure and BP soft crystals, core−shell droplets of different sizes (R_{out}), and average shell thicknesses (h) were prepared using the capillary microfluidics (Figure 1B). Then the effect of surface anchoring, geometrical confinement and curvature on the packing of DTCs and 3D lattice structure of BPs in nano/microscale was systematically investigated. The results were translated into their optical responses.

Effect of Surface Anchoring. We have studied the impact of surface anchoring on the orientational transition and phase behavior of the high-chirality liquid crystal on 4.0 ± 1.0 μm thick shells with a thickness (h) to radius (R_{out}) ratio of 0.1 ± 0.01. Shells with relatively similar outer diameters were selected for this study to ensure surfaces with constant Gaussian curvature. Shells with all possible surface anchoring conditions were prepared, *i.e.*, degenerate planar at both interfaces (P(in)−P(out)), homeotropic at both interfaces (H(in)−H(out)), degenerate planar at the inner and homeotropic at the outer interface (P(in)−H(out)), and vice versa (H(in)−P(out)) (Figure 1E−H)). The surface anchoring was controlled using poly(vinyl alcohol) (PVA) and sodium dodecyl sulfate (SDS) at concentrations that induce strong degenerate planar and homeotropic anchoring, respectively (Figure 1D). For producing the degenerate planar−planar shells, 15 and 10 wt % PVA solutions were used for the inner and outer phases, respectively. Degenerate planar surface anchoring causes chiral molecules to lie

https://doi.org/10.1021/acsnano.2c02799
ACS Nano 2022, 16, 15894−15906

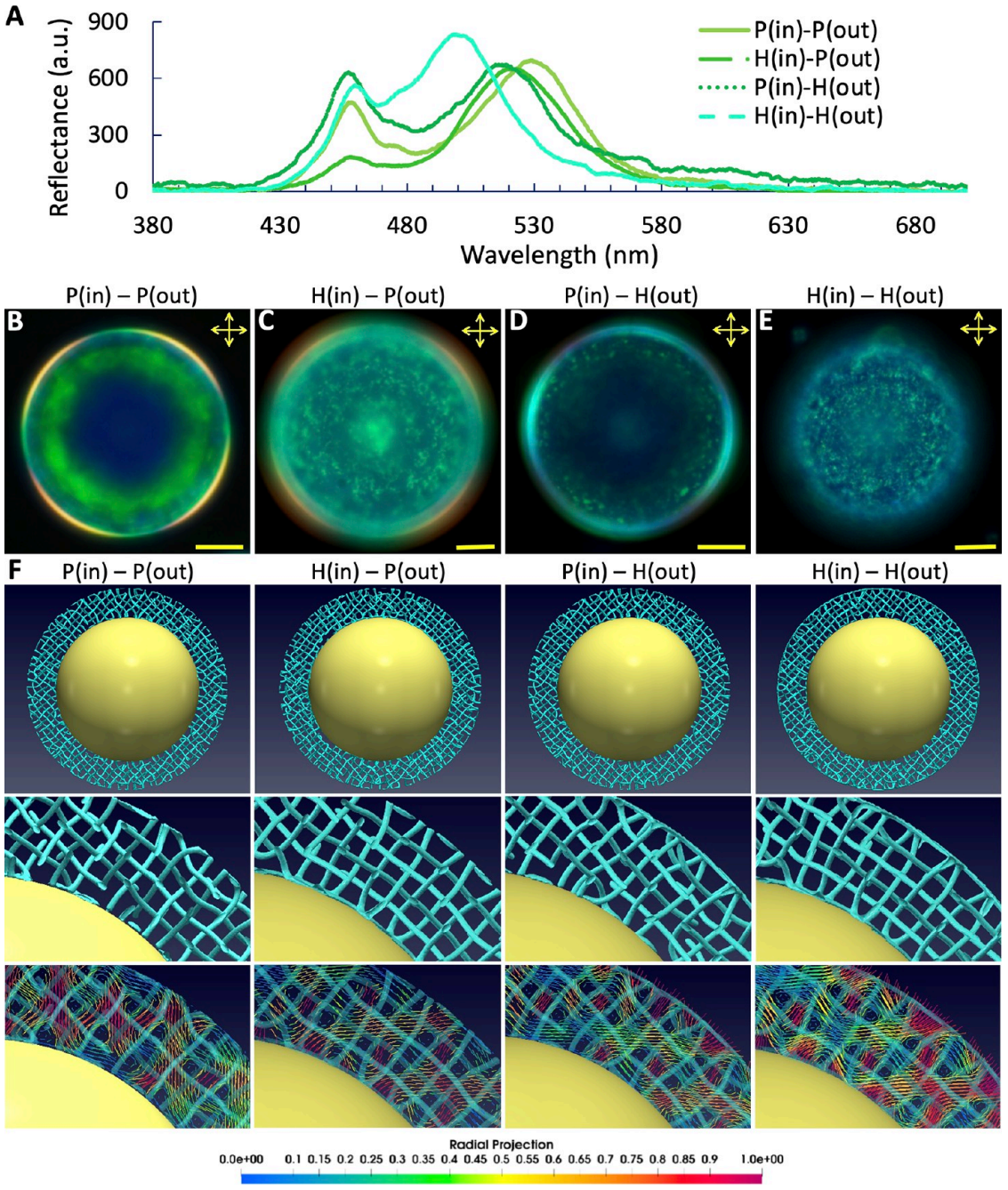

Figure 2. Effect of homeotropic surface anchoring on the structural stability of BPI. (A) Blue-shift in diffused spectra pattern of BPI shell with at least one homeotropic surface boundary. Cross-polarized reflected light micrographs of BPI shell with surface anchoring of (B) P(in)−P(out), (C) H(in)−P(out), (D) P(in)−H(out), and (E) H(in)−H(out) (scale bar = 20 μm). (F) Snapshots of a cross-section of the simulated disclination lines of BPI shell (h/p = 2) exposed to different boundary conditions. The disclination lines are visualized as green tubes in the magnified section, which correspond to regions with scalar order parameter <0.5. The director field indicates the preferred molecular alignment where the color map goes from blue to red according to the radial projection of the local director.

tangentially on the aqueous interface and aligns the twist axis normal to the surface, with no frustration, forming a radial structure with a cross pattern feature under a polarized microscope (Figure 1E).[28] Homeotropic surface anchoring, on the other hand, orients molecules perpendicular to the interface, leading to parallel alignment of the twist axis to the interface, which is incompatible with the normal alignment of the twist axis in bulk (Figure 1F). The homeotropic−homeotropic boundary condition was achieved using 10 and 5 wt % SDS solutions for the inner and outer phases, respectively. Homeotropic boundary condition at both concave and convex interfaces of the shells induces further frustration, leading to the formation of focal conic domains with irregular polygonal patterns, where the normal alignment of the liquid crystal molecules at the interfaces competes with the preferred in-plane orientation of the cholesteric layers in bulk (Figure 1F).[36]

By altering the surface anchoring conditions, we prepared shells with hybrid surface anchoring inducing different molecular organizations at the inner and outer surfaces (Figure

https://doi.org/10.1021/acsnano.2c02799
ACS Nano 2022, 16, 15894−15906

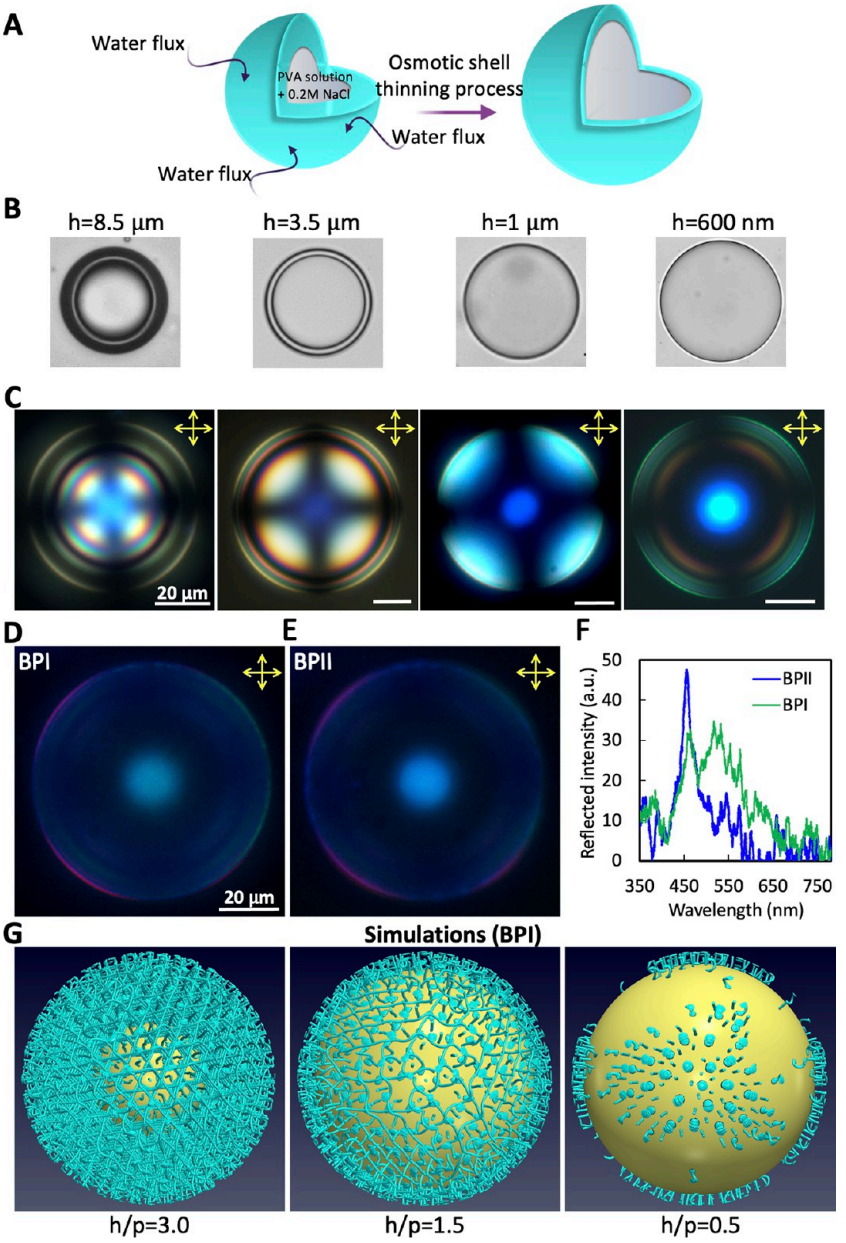

Figure 3. Reducing the shell thickness using the osmotic stretching process in shells with degenerate planar anchoring at inner and outer interfaces reconfigures the cholesteric structure and destabilizes BPI. (A,B) Schematic of the osmotic thinning process and bright-field micrographs of cholesteric shells with different shell thicknesses. (C) Reflection-mode cross-polarized micrographs of cholesteric shells with different shell thicknesses. (D,E) Reflection-mode cross-polarized micrographs of BPI and BPII in 1 μm thick shells, and (F) the corresponding reflection spectra, and (G) snapshot of simulated defect lines in the BPI shell with degenerate planar anchoring at inner and outer confining interfaces and shell thickness to pitch length ratio h/p of 3, 1.5, and 0.5.

1G,H). In the cholesteric phase, shells with inner degenerate planar anchoring and outer homeotropic anchoring exhibit hexagonal/pentagonal focal conic domains covering the outer surface (Figure 1G and the inset). These domains become larger as the shell thickness increases (SI, Figure S2). Focal conic domains emerge at homeotropic interfaces where cholesteric layers with different twist axes approach each other while bending around two focal lines normal to the interface (SI, Figures S3 and S4).[36,45] This unique feature of molecular arrangement will be discussed in more detail in the next section. Changing the surface anchoring order (H(in)−P(out)), however, generates an oily streak appearance on the outer surface and irregular polygonal focal conic patterns on the inner core surface (Figure 1H and the inset). Compared to Figure 1G, their diverse polygonal shapes can be associated with the handedness mismatch of the twisted cholesteric layers and convex curvature of the core interface.

We further investigated the effect of surface anchoring conditions on the crystallization, phase behavior, and the optical response of the BP structures strained within shell boundaries (Figure 1E−H). The results show that imposing homeotropic surface anchoring on the outer boundary shifts the BP transition temperatures by about 1.4 °C, approaching the transition temperatures of the film (Figure 1C). Moreover, compared to the shells with two degenerate planar interfaces, confining BPI with at least one homeotropic surface boundary

https://doi.org/10.1021/acsnano.2c02799
ACS Nano 2022, 16, 15894−15906

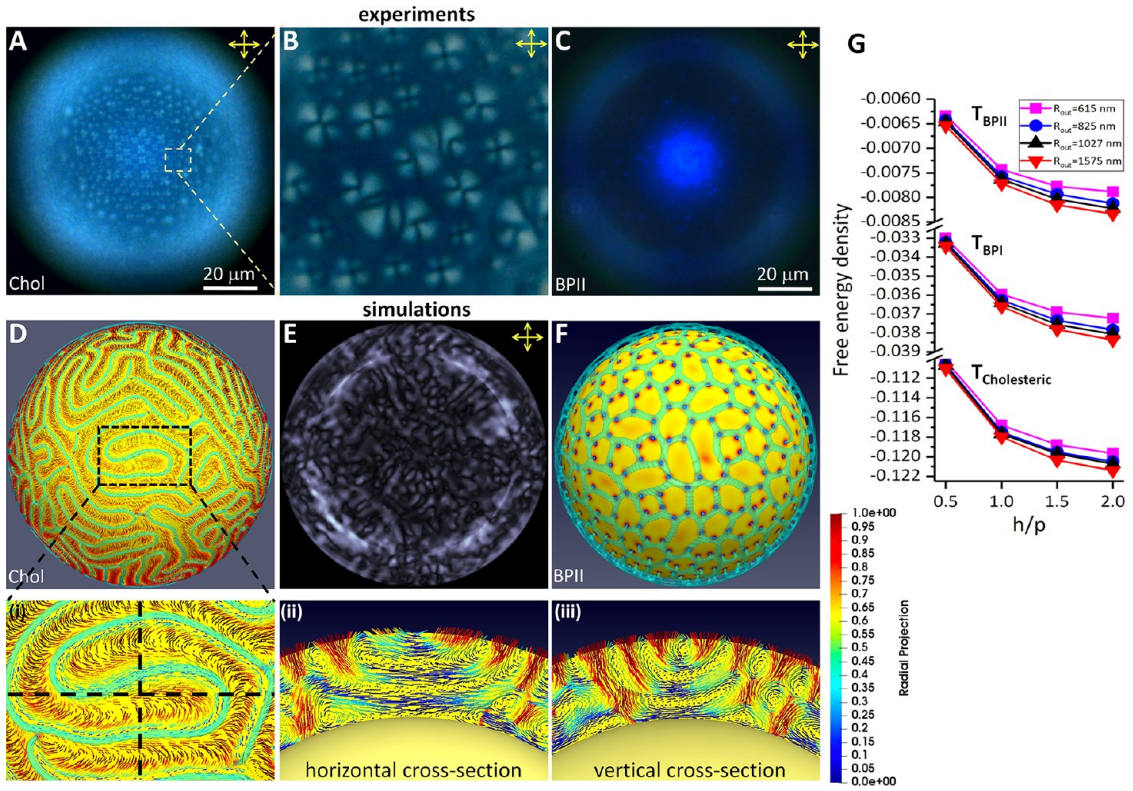

Figure 4. Cholesteric structure and BPII in a 1 μm thick shell with hybrid surface anchoring, P(in)−H(out). (A,B) Reflection-mode cross-polarized micrographs of hybrid shell in cholesteric phase and a magnified image of the focal-conic patterns, and (C) reflection-mode cross-polarized micrographs of a BPII shell. (D) Snapshot of the simulated defect lines of the cholesteric shell with hybrid P(in)−H(out) surface anchoring (h/p = 1.5). Double spirals are the signature of focal conic domains; these patterns are formed near the homeotropic surface of the shells. (D(i−iii)) Zoom-in of the director field at a focal conic domain and the vertical and horizontal cross sections. The color map of the director field goes from blue to red depending on the radial projection of the directors ($n \bullet \hat{r}$). (E) Snapshot of the simulated transmission-mode cross-polarized micrograph of the cholesteric shell with hybrid P(in)−H(out) surface anchoring (h/p = 1.5), and (F) snapshot from the simulated director field orientation of $BPII_{(100)}$ shell. (G) free energy density in reduced units ($f^* = f/L\xi$, with L the elastic constant and ξ the coherence length) as a function of confinement ratio, h/p for different shell sizes (R_{out} is the outer radius of the core−shell droplet) in the cholesteric phase (U = 5.0), BPI (U = 3.5), and BPII (U = 2.755). At BP thermal conditions, strong shell confinement favors the formation of skyrmion-like structures.

blue-shifts the reflection spectrum. The magnitude of the shift in the reflected wavelength was approximately 8, 12, and 30 nm for shells with surface anchoring conditions of H(in)−P(out), P(in)−H(out), and H(in)−H(out), respectively (Figure 2A−E). The blue-shift becomes more pronounced as the portion of the homeotropic surface anchoring increases.

A detailed computational analysis was performed to understand the balance between the curvature-induced strain and surface anchoring on the BP lattice structures and DTCs arrangement and the origin of the blue-shift in BPI shells (Figure 2F). Our experimental studies and computational simulations have shown that the light reflection at 530 and 450 nm are, respectively, associated with [110] and [100] lattice planes of BPI and BPII structures with lattice parameters of a_{BPI} = 250 nm and a_{BPII} = 150 nm.[44] Here, mean-field continuum simulations were implemented for BPI shells at all different surface anchoring combinations; P(in)−P(out), H(in)−P(out), P(in)−H(out), and H(in)−H(out). To determine the effect of curvature, the results were compared to the case when the liquid crystal is confined in thin flat films. In a flat film with a thickness larger than the chiral pitch, p $\left(\frac{h}{p} \gtrsim 1.5\right)$, BPI disclination lines slightly bend and approach each other near the homeotropic interface (SI, Figure S5). In shells, on the other hand, the coupling of curvature and homeotropic surface frustration disrupts the BPI lattice periodicity, forcing it to shrink and form junctions of disclination lines near the interface (Figure 2F), resulting in a blue-shift in the reflectance spectra. In contrast, regardless of the surface anchoring, the reflected color in BPII shells remains unchanged at 450 nm, indicating higher structural integrity of BPII and an ability to adjust to curved spatial confinement (Figure 1E−H, SI, Figures S6−S7).

Effect of Shell Thickness. The shell thickness was controlled using the osmotic swelling process. By adding 0.2 M NaCl into the inner aqueous phase, the water flux was directed toward the inner core, thereby reducing the shell thickness (Figure 3A,B). In shells with degenerate planar anchoring at both confining interfaces, reducing the thickness to 600 nm significantly affects the molecular arrangement and optical features despite being above the BP unit cell size (Figure 3C). In the cholesteric phase, the geometrical frustration mediates the twist deformations, leading to a significant decrease in the optical intensity of reflected light (Figure 3C). Moreover, the crossed-polarized image in the transmission mode exhibits the extension of a large dark spot in the center of the thin shell, resembling the nematic-like radially oriented morphology with a Maltese cross pattern (SI,

https://doi.org/10.1021/acsnano.2c02799
ACS Nano 2022, 16, 15894−15906

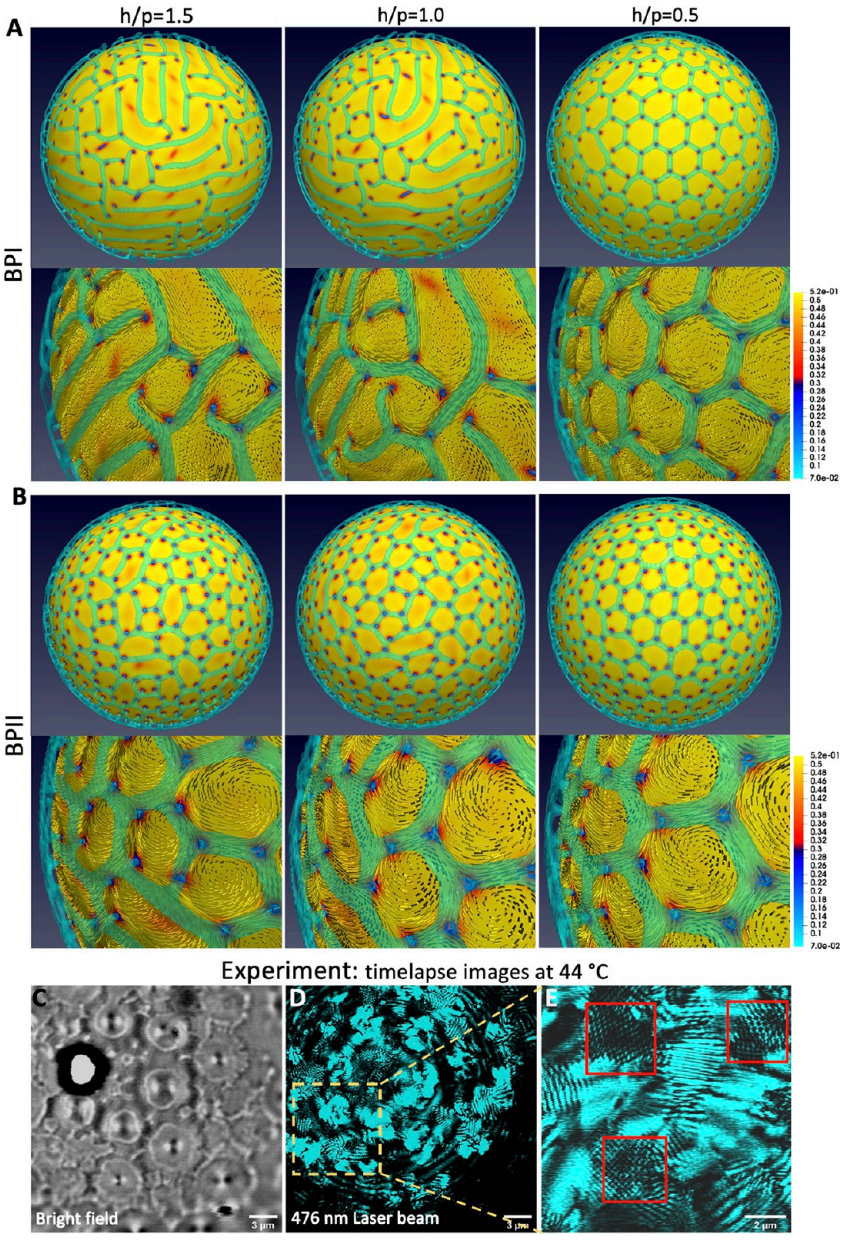

Figure 5. Half-skyrmion lattices form in shells with hybrid surface anchoring (P(in)−H(out)) upon decreasing the thickness. (A,B) snapshot of director field and isosurfaces of the scalar order parameter of BPI and BPII shells and their magnified view upon reducing the thickness from 1.5*p* to 0.5*p*. (C−E) Timelapse super-resolution confocal laser scanning microscopy taken at the temperature at which structural transitions from (C) cholesteric to (D) BPs take place in a shell with a thickness of 600 nm, (E) magnified images of a selected region in (D).

Figure S8). BPI and BPII appear consecutively in thick shells upon increasing the temperature. However, reducing the shell thickness to about 1 μm makes differentiating two mesophases difficult (Figure 3D,E); they show diffused reflection spectra with broadband reflection peaks (Figure 3F). According to our computational simulations, increasing the confinement to h/p = 0.5 (h = 130 nm) in shells with degenerate planar interfaces distorts the BP unit cells and diminishes light intensity (Figure 3G). In experiments, however, the coupling of curvature and spatial confinement hinders the BP crystals' nucleation at a thickness and h/p larger than those accessible in simulations (h = 600 nm).

As discussed before, altering the anchoring of the outer surface from degenerate planar to homeotropic (hybrid-aligned shells) generates focal conic domains on the surface of the cholesteric shells (Figure 1G, Figure 4A,B), which is consistent with our computational simulations and previous studies (Figure 4D)).[35,36] In fact, focal conic domains form when cholesteric layers with different twist axis meet each other and bend around two focal lines to become normal to the interface (SI, Figure S3). The disclination lines of a focal conic domain on curved surfaces, including shells, exhibit a double spiral pattern (Figure 4D(i) and SI, Figure S4). Therefore, the double spiral arrangement of the disclination lines on the shell's interface is considered the sign of a focal conic domain.[36,45] The director field of a double spiral region and its vertical and horizontal cross sections presented in Figures 4D(i−iii) demonstrate how cholesteric layers with different twist directions meet, bend, and form a focal conic domain. Figure 4E represents the cross-polarized micrograph of the

https://doi.org/10.1021/acsnano.2c02799
ACS Nano 2022, 16, 15894−15906

simulated hybrid-aligned shell (Figure 4D). The discrepancy between the cross-polarized images of the experiment and computational simulations (Figure 4A,E) is attributed to the polarization mode and the presence of stripe patterns in the simulated hybrid-aligned shells. In fact, the simulated crossed-polarized image is taken in the transmission mode, which can be influenced by the arrangement of the liquid crystal molecules through the bulk. In the experiment, however, the cross-polarized images (Figure 4A,B) are recorded in the reflection mode showing the interaction of the polarized light with liquid crystal molecules arranged into double spiral domains on the surface.

We have further found that reducing the shell thickness to 1 μm increases the number of focal conic domains and decreases their size considerably (Figure 4A, SI, Figure S2). Upon further decreasing the shell thickness (700 nm), focal conic domains are accompanied by stripe patterns (SI, Figures S4, S9, and S10). The stripe patterns that form due to the interplay of cholesteric layers and curvature of the interface are clearly predicted by computational simulations (Figure 4D). In these patterns, the director field exhibits the radial spherical structure at the proximity of the inner degenerate planar interface, which changes abruptly near the outer homeotropic interface, forming +1/2 disclination lines (SI, Figure S10). Because the computational simulations are limited to overall smaller shell sizes than experiments, the stripe patterns coexist with focal conic structures at higher shell thicknesses, which is attributed to the pronounced curvature effect (Figure 4D). We discuss the role of curvature in the next section.

Upon raising the temperature in thin hybrid-aligned shells (1 μm thick), the cholesteric structure directly transitions to BPII, without showing BPI optical features (Figure 4C). The instability of the BPI structure under curved strong confinement can be attributed to its larger lattice unit size than BPII. According to our computational analysis, homeotropic anchoring yields a regular orientation of the anisotropic molecules in the form of a submicrometric cross-pattern on the shell's surface, which is observed at greater thicknesses ($h/p \approx 1.5$) than those reported in thin films ($h/p < 0.5$). The simulation snapshot shown in Figure 4F corresponds to the near-surface disclination lines and scalar order map of a BPII shell.

To better understand this phenomenon, the free energy of the structures at temperatures corresponding to BPs in bulk was analyzed in the thin hybrid-aligned shells as a function of h/p (Figure 4G). As explained in the Methods section, under the mean-field Landau−de Gennes framework, the free energy functional is minimized for the tensor order parameter $\mathbf{Q}$, which contains information about the structure of the phase. This minimization process depends on the initial conditions. Given the abundance of possible metastable states, it is crucial to start from the ansatz of BPs to analyze the morphologies that emerge under confinement. Regardless of the shell size, at temperatures where BPs are observed in bulk (*i.e.*, $U = 2.755$ for BPII and $U = 3.5$ for BPI, see the Methods section), our computational results show a lower total free energy density for simulations starting from an initial BPII configuration. Although we observe higher structural stability for BPII in thin shells, skyrmion-like lattices nucleate approaching $h/p \approx 1.5$, below which BP morphologies become unstable. Therefore, the dots shown in Figure 4F correspond to skyrmion structures formed at the BPII and BPI thermal conditions (see Figure 5A,B). Moreover, the growth rate of the density free energy is more pronounced for the BP regime than for the cholesteric regime. This behavior is associated with the crystalline symmetry distortion of BPs induced by the curvature and confinement strain (Figure 4G).

Although BPII shows higher stability than BPI, in the experiment, reducing the shell thickness to <700 nm destabilizes both structures, resulting in a faded blue color with a broad spectral width (SI, Figure S9). To determine the structural arrangement, shells with a thickness of 600 nm were characterized by super-resolution confocal laser scanning microscopy, CLSM (Figure 5C). At the temperature where the cholesteric to BP transition takes place, CLSM with a laser beam of 476 nm reveals the melting of focal conic structures and the formation of periodic hexagonal patterns on the shell surface. These patterns with nanoscale lattice constants of around 300 nm do not match the unit cell size of BPI (250 nm) or that of BPII (150 nm). Instead, they correspond to the characteristic length scale of half-skyrmion patterns in BPs.[29,30]

To shed light on the experimental measurements and understand the arrangement of the disclination lines in BPs within thin shells, we turned again to computational simulations of shells with confinement ratio h/p of 1.5, 1, and 0.5 (Figure 5A,B). We find that for a shell thickness of $1.5p$, the skyrmion structures with a lattice constant of 300 nm nucleate at temperatures where BPs would form in bulk, which is in quantitative agreement with the results of CLSM (Figure 5C). On the spherical surface, the director rotates $\pi/2$ from the center to the perimeter of the skyrmion (Figure 5 and SI, Figure S11).[46,47] In addition, our results indicate that upon reducing the shell thickness below p ($h < p$), both BPI and BPII tend to adopt the same configurational order, resulting in a similar optical feature (Figure 5 and SI, Figure S9). By reducing the shell thickness to half a pitch length, the hexagonal network of disclination lines forms throughout the BP shells, reminiscent of half-skyrmions textures. This structure was previously reported by Zumer and Fukuda for BPs confined in a 2D flat film with thickness below the chiral liquid crystal pitch length.[29] Our experimental and computational results, however, demonstrate that the coupling of curvature, spatial confinement, and surface anchoring can trigger the formation of skyrmion structures at higher thicknesses compared to a quasi-2D flat film.[29−31] In contrast to the skyrmion lattices formed in a flat channel, the formation of the uniform hexagonal lattice, which would correspond to skyrmion particles surrounded by six −1/2 topological defects, is not plausible under spherical confinement. We computed the bond orientational order parameter (BOP) for shells with R = 615, 825, 1027, and 1575 nm to characterize the possible structures (Table 1). To do so, we calculated the average of

Table 1. BOP for Different Shell Sizes and $h/p = 0.5$ and $U = 2.755$[a]

R\BOP	$n = 5$	$n = 6$	$n = 7$	$n = 8$
615 nm	0.184	0.755	0.061	0
825 nm	0.185	0.697	0.118	0
1027 nm	0.166	0.725	0.098	0.011
1575 nm	0.142	0.731	0.127	0

[a]The values obtained indicate that the skyrmion lattices are mostly formed by hexagonal and pentagonal arrangements. BOPs for $n < 5$ and $n > 8$ were not observed. Note that for a shell thickness, $h/p = 0.5$ BOP with $n = 8$ only appears in large droplets.

https://doi.org/10.1021/acsnano.2c02799
ACS Nano 2022, 16, 15894−15906

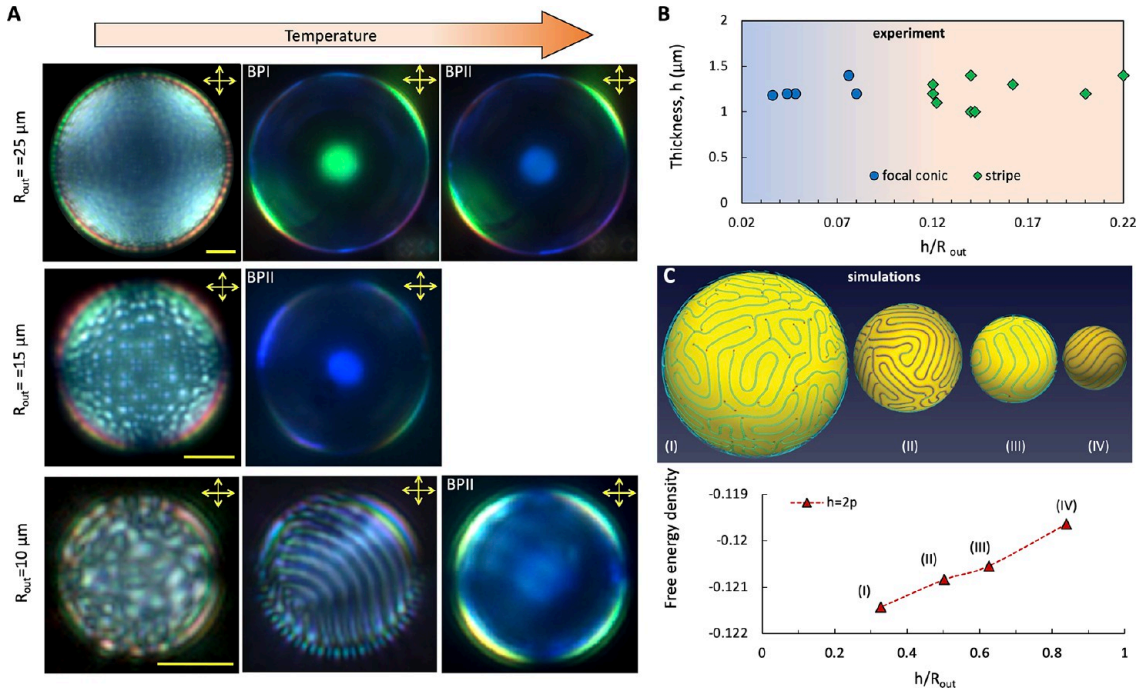

Figure 6. Increasing the curvature of the confined space in hybrid P(in)−H(out) shells triggers the transition of focal-conic structure to stripe patterns and destabilizes BPI. (A) Reflection-mode cross-polarized light micrographs of cholesteric and BP shells with an outer radius of 25, 15, and 10 μm (scale bar = 10 μm). (B) Phase diagram in the cholesteric shell as a function of shell thickness, h, to outer radius ratio (h/R_{out}). (C) Snapshots of the simulated defect lines and free energy density in reduced units as a function of h/R_{out} in cholesteric shells (constant shell thickness, $h = 2p$).

$|\Psi_n|^2 = \Psi_n\Psi_n^*$, where $\Psi_n(r_i) = \frac{1}{N_i}\sum_{j=0}^{N_i} e^{ni\theta_{ij}}$, θ_{ij} is the angle between an arbitrary fixed direction and the vector connecting the center of the skyrmion particle i and j, and N_i is the number of nearest neighbors. The BOP is a measure of the present arrangements of the lattices obtained. For example, $|\Psi_6| = 1$ indicates a perfect hexagonal lattice. The results show that, regardless of the shell radius, $|\Psi_6|$ is the dominant value followed by $|\Psi_5|$, which indicates that skyrmions are mostly distributed in hexagonal and pentagonal arrangements on the shell surface. These symmetries can also be identified by the polygons formed by the disclination lines that connect the −1/2 defects on the surface of the shells as shown in Figure 5.

Effect of Shell Curvature. Shells having the same thickness, but different diameters were prepared to investigate the impact of Gaussian curvature on the organization of the high-chirality liquid crystal molecules in the cholesteric phase and BPs. The effect of curvature was examined for degenerate planar-planar shells as well as the hybrid-aligned ones with homeotropic anchoring at the outer interface.

In shells with degenerate planar surfaces, cross-polarized images in the reflection mode reveal no detectable changes in the molecular order of the cholesteric phase with shell diameter. The bright spot that appears in the center of the transmission mode cross-polarized images of the shells can be attributed to the optical interference with curved surfaces (SI, Figure S12). Moreover, BPI and BPII appear consecutively upon raising the temperature, and their crystal lattices and optical responses remain almost unchanged regardless of the shell diameter.

In contrast, the cross-polarized images of the hybrid shells with inner degenerate planar and outer homeotropic surface anchoring reveal a distinct reconfiguration in molecular ordering upon reducing the shell diameter (Figure 6A). Increasing the Gaussian curvature significantly affects the orientational order in the cholesteric phase, and the focal conic domains transition into bend stripe patterns (Figure 6, SI, Movie S1). Varying the shell curvature shows the existence of two thermodynamically distinct textures in the cholesteric phase (Figure 6B). According to our experimental results, for $0.11 < h/R_{out}$ (R_{out} is the outer radius of the core−shell droplet), the bending stripe patterns develop on the cholesteric shells (Figure 6A,B). Beyond this window, however, decreasing the curvature induces the focal conic pattern formation. These results are in quantitative agreement with the computational simulations (Figure 6C), demonstrating instability of the focal conic structures at large degrees of curvature with higher free energy density and thereby their transformation into stripe patterns. Our simulation results also show that stripes and focal conic domains coexist for shells of diameter 2054 and 3150 nm, while the stripe pattern becomes dominant for smaller sizes. We have also explored the effect of curvature on the BP behavior in the hybrid-aligned shells. We find that reducing the outer shell radius hinders the formation of BPI, which can be attributed to its larger lattice size and disconnected defect lines.

CONCLUSIONS

The crystallization of Blue Phases has been examined within a shell geometry as a function of size and surface anchoring. The experimental studies were complemented by computational simulations to provide an understanding of the coupled effects of curvature, confinement, and surface anchoring. Our results demonstrate that cholesteric shells with homeotropic surface anchoring on at least one of the two boundaries form a focal conic structure on the surface, which transforms to stripe-like patterns as the shell curvature increases. We have found that

https://doi.org/10.1021/acsnano.2c02799
ACS Nano 2022, 16, 15894−15906

homeotropic anchoring deforms the BPI-unit cell at the shell surface, leading to a blue-shift in the reflectance spectra. According to our experimental and computational results, a higher curvature and strong spatial confinement destabilize BPI and reconfigure it to adopt the structure of BPII. The instability of BPI within curved confinement can be attributed to its larger lattice size and disconnected disclination lines.

We have also found that confinement within curved spaces can trigger the formation of skyrmion lattices at greater thicknesses than those reported for a flat geometry. Overall, these findings demonstrate that the coupling of curvature, confinement, and elasticity of the cholesteric and BP liquid crystals under various anchoring conditions can affect their structural stability leading to the emergence of exotic molecular configurations. This fundamental knowledge will be of use for the design of BP-based miniaturized and flexible devices and materials, including fiber optics, wearable sensors, and smart fabrics.

METHODS

Experiment. The BP mixture was composed of 37 wt % chiral additives (S811, 2-octyl 4-(4-hexyloxybenzoyloxy) benzoate, Merck) and 63 wt % nematic liquid crystal (MLC2142; 1-methyl-4-(4-*trans*-vinyl-[1,1′-bicyclohexyl]-4′-trans-yl)-benzene, 2-(2-hydroxy-5-methylphenyl)-2*H*-benzotriazole, EMD Chemicals). The mixture was prepared by the cosolvent method, in which the solvent was evaporated afterward using a rotary evaporator. Aqueous solutions of poly(vinyl alcohol) (PVA, 13K−23K, and 87−89% hydrolyzed; Sigma-Aldrich) and sodium dodecyl sulfate (SDS, >98% purity; Sigma-Aldrich) were used to induce degenerate planar or homeotropic alignment on each side of the shell surface, respectively. Sodium chloride (Sigma-Aldrich) and glycerol (Acros Organic) were added to the aqueous phase to adjust the shell thickness through the osmotic thinning process. We used 2-[methoxy (polyethyleneoxy)-propyl] trimethoxysilane (Gelest) and dimethyloctadecyl [3-(trimethoxysilyl) propyl] ammonium chloride (DMOAP, 72% purity; Sigma-Aldrich) to render the glass capillary surface hydrophilic and hydrophobic, respectively.

Core−shell droplets composed of high-chirality liquid crystal were prepared using a microfluidic setup. The microfluidic device was designed using a combination of coflow and flow-focused geometry following Weitz *et al.*[48] Two round borosilicate capillaries (0.58 mm ID and 1 mm OD, WPI) were tapered by a micropipette puller (P2000, Sutter Instrument, Novato, CA, US). Microforge (Narishige, MF-900, Japan) was used to adjust the opening of the injection and collection capillaries to control the outer diameter of the shells. The injection capillary was surface modified using 1 wt % aqueous DMOAP solution to render it hydrophobic. The tapered capillaries were aligned inside a square tubing (1.05 mm ID and 1.50 OD, Harvard square tubing) with a separation distance of 300 μm. The square and collection capillaries were modified by 2-[methoxy (polyethyleneoxy) propyl] trimethoxysilane to render their surface hydrophilic. They were then assembled on a precleaned glass slide, and 20 gauge needles were used to inject phases into the capillaries (Figure 1B).

The inner phase (core) of the core−shells was injected through the hydrophobic capillary. The liquid crystal as the middle phase was injected through the space between the hydrophobic and square capillaries. The outer phase was injected through the gap between the hydrophilic and square capillaries (Figure 1B). Three syringe pumps (Elite 11 series, Harvard Apparatus, Holliston, MA) were used to set the flow rates at 200, 100, and 4000 μL/h for inner, middle, and outer phases, respectively. The inner and middle phases flow in the same direction (co-flow), and they were flow-focused by the continuous phase. In other words, the innermost aqueous phase is encapsulated by the liquid crystal shell, which becomes dispersed in the outer phase (continuous phase).

In liquid crystal shells, the middle phase (liquid crystal) is surrounded by aqueous phases. Thereby, the liquid crystal alignment on each surface can be controlled by surface-active agents. To manipulate the surface alignment on the shell, different surfactants in water−glycerol mixture solutions (80:20 volume ratio) were examined. The hybrid-aligned shells were produced using two different surfactants for the inner and outer phases. The shell thickness was adjusted by changing the flow rates and carrying out the osmosis thinning process. In this process, the innermost aqueous phase contains 0.2 M NaCl to generate an osmolarity difference of around 0.98 osmol/L.[49]

The bright field and crossed-polarized images of the core−shells were obtained by a Zeiss Axioscope 5 microscope (Oberkochen, Germany) in transmission and reflection modes with 50× and 100× objective lenses. The reflectance spectra of samples were measured by fiber optic spectrometer (Flame UV−vis, Ocean Insight). Conoscopy technique was employed to determine the Kossel diagrams of the BP crystal structures in the BP films. BP films were made by capillary filling of cells composed of two coverslips separated by a 12 μm spacer. In this technique, a highly convergent monochromatic beam illuminates a single BP domain. Due to the BP crystalline symmetries, the ordered patterns identifying the BPI and BPII lattice planes are created at the back focal plane of the objective, which can be detected by a Bertrand lens. To achieve a highly convergent light beam, we used a filter with a bandpass of 500 nm (Thorlabs, New Jersey, US) and an objective lens with a high numerical aperture (100×, NA = 1.3). To image the periodic structure of the double-twisted cylinders in the BP shells, a Leica TCS SP5 II STED laser scanning confocal microscope (super-resolution confocal laser scanning microscopy, Leica Microsystems, Inc., Buffalo Grove, IL) with a 100× oil objective lens was used. The confocal micrographs were obtained in a reflection mode, and the reflected light was passed through a 26 μm pinhole disk to physically obscure out-of-focus light. The interaction of the 476 nm laser beam with the BP periodic structure gives rise to Bragg reflection, revealing the internal structure of the label-free BPs in shells. The transition temperatures of core−shells were recorded by a Linkam heating stage T-96, mounted on the microscope stage. The transition temperatures were measured upon heating/cooling cycles with a rate of 0.2 °C/min. To prepare the sample cells, the label-free core−shells were collected in lab-built wells made of two coverslips (no.1) separated by a 100 μm thick PDMS spacer ring.

Theoretical Modeling. We employed the adjusted continuum mean-field Landau−de Gennes free energy model to describe the liquid crystalline system.[50−52] Free energy of the system is associated with the second-rank order tensor parameter, which is defined by

$Q_{ij} = S(n_i n_j - \frac{1}{3}\delta_{ij})$Here, i,j are local director components, S is a scalar order parameter, and δ is the identity tensor. The Q-tensor is symmetric and traceless. In this regard, the total energy function is given by[41]

$$F(Q) = \int d^3x[f_L(Q) + f_E(Q)] + \int d^2x f_s(Q)$$

Total free energy is the result of three energy contributions named short-range free energy f_L, long-range free energy f_E, and surface anchoring energy f_S. These free energy components are defined as follows:

$$f_L = \frac{A}{2}\left(1 - \frac{U}{3}\right)tr(Q^2) - \frac{AU}{3}tr(Q^3) + \frac{AU}{4}tr(Q^2)^2$$

where, A and U are material-specific parameters, which are correlated with energy scale and nematic−isotropic transition, respectively. We used U = 5.0, 3.5, and 2.755 for Chol, BPI, and BPII conditions, respectively. The long-range energy contribution is defined by

$$f_E = \frac{1}{2}L\left[\frac{\partial Q_{ij}}{\partial x_k}\frac{\partial Q_{ij}}{\partial x_k} + 2Lq_0\epsilon_{ikl}Q_{ij}\frac{\partial Q_{lj}}{\partial x_k}\right]$$

Here, L is an elastic constant, and q_0 defines the chirality of the system, and it is defined by $q_0 = \frac{2\pi}{p}$ and ϵ_{ikl} is the Levi−Civita tensor.

https://doi.org/10.1021/acsnano.2c02799
ACS Nano 2022, 16, 15894−15906

The surface energy contribution depends on the anchoring conditions. For a degenerate planar, it is given by

$$f_s = W_P(\tilde{Q}_{ij} - \tilde{Q}_{ij}^{\perp})^2$$

where, W_P is degenerate planar anchoring strength, $\tilde{Q}_{ij} = Q_{ij} + \frac{1}{3}S_{eq}\delta_{ij}$ and S_{eq} is defined as $S_{eq} = \frac{1}{4}\left(1 + 3\sqrt{1 - \frac{8}{3U}}\right)$. $Q_{ij}^{\perp}$ is the projection of $\tilde{Q}_{ij}$ on the surface and is defined as $Q_{ij} = P_{ik}\tilde{Q}_{kl}P_{ij}$ and $P_{ij} = \delta_{ij} - \nu_i\nu_j$. For homeotropic anchoring, the surface free energy density is,[42]

$$f_s = W_H(Q - Q_0)^2$$

where W_H is the homeotropic anchoring energy, and Q^0 is the tensor order parameter corresponding to an alignment normal to the surface. For the present study, we use p = 258 nm, $W_P = 4 \times 10^{-3}$ Jm^{-2} and $W_H = 8 \times 10^{-4}$ Jm^{-2}, $A = 1.067 \times 10^5$ Jm^{-3} and L = 6 pN. The minimization process was achieved using the finite difference method in a grid box of mesh resolution of a coherence length (ξ = 7.5 nm).

Stable and metastable states were analyzed by minimizing the free energy equation by means of Ginzburg–Landau relaxation, which is expressed by

$$\frac{\partial Q}{\partial t} = -\frac{1}{\gamma}\left[\Pi\left(\frac{\partial F}{\partial Q}\right)\right]$$

where γ is a diffusion parameter and the operator Π ensures that the Q-tensor preserves the symmetry and traceless properties, and it is given by $\Pi(\mathcal{A}) = \frac{1}{2}(\mathcal{A} + \mathcal{A}^T) - \frac{I}{3}tr\mathcal{A}$. Because the LC is confined, the boundary conditions for the evolution of the Q-tensor satisfy $\left[\Pi\left(\frac{\partial F}{\partial \Delta Q}\right)\bullet\nu\right] = 0$ where ν is the normal vector to the shell surfaces.

Initial configuration for BPI and BPII can be obtained as follows,[43,52]

BPI:

$$Q_{xx} = a\left(-\sin\left(\frac{ky}{\sqrt{2}}\right)\cos\left(\frac{kx}{\sqrt{2}}\right) - \sin\left(\frac{kx}{\sqrt{2}}\right)\cos\left(\frac{ky}{\sqrt{2}}\right) + 2\sin\left(\frac{kz}{\sqrt{2}}\right)\cos\left(\frac{ky}{\sqrt{2}}\right)\right)$$

$$Q_{xx} = a\left(-\sin\left(\frac{kx}{\sqrt{2}}\right)\cos\left(\frac{kz}{\sqrt{2}}\right) - \sin\left(\frac{ky}{\sqrt{2}}\right)\cos\left(\frac{kz}{\sqrt{2}}\right) + 2\sin\left(\frac{kx}{\sqrt{2}}\right)\cos\left(\frac{ky}{\sqrt{2}}\right)\right)$$

For BPII:

$$Q_{xx} = a(\cos(kz) - \cos(ky))$$

$$Q_{xy} = a\sin(kz)$$

In all cases, the components yy, zz, xz, and yz are obtained by the corresponding cyclic permutation, and the amplitude of initialization is a = 0.2 and $k = 2q_0r$, where r is the red-shift. The red-shift is related to BPs lattice parameter and the chiral pitch *via* $a_{BPI} = p/\sqrt{2}r$ and $a_{BPII} = p/2r$ with r = 0.71 for BPI and r = 0.86 for BPII. The director corresponds to the eigenvector of the Q-tensor with the largest eigenvalue. A picture of the initial conditions of BPs can be found in the SI, Figure S13.

For each anchoring condition, we have considered the following configurations: random, uniform, and the ansatz of the radial spherical structure, RSS, which is given by[23]

$$n(r, \phi, \theta) = \cos\Omega e_r + \sin\Omega e_\phi \text{ with } \Omega = q_0 z$$

where $e_r$and e_ϕ are the unit vectors in spherical coordinates (r, ϕ, θ), q_0 is the chirality strength $q_0 = \frac{2\pi}{p}$ and z is defined as the symmetry axis in rectangular coordinates. The free energy densities for each case were compared, and the one with the lowest value was taken as the stable configuration.

ASSOCIATED CONTENT

Supporting Information

The Supporting Information is available free of charge at https://pubs.acs.org/doi/10.1021/acsnano.2c02799.

Reflectance spectra of BPI and BPII phases in a 12 μm thick film, focal conic domains in shells with different thicknesses, definition, model and snapshot of the director field in focal conic domains in cholesteric films and shells with homeotropic surface anchoring, simulation results of the disclination lines formed by confinement of a ChLC, with p = 258 nm, in thin channels at the BPI-temperature regime, disclination lines formed by confinement of a ChLC (p = 258 nm) in thin channels at the BPII-temperature regime, reflectance spectra of BPII shells with different surface anchoring, cross-polarized micrographs of a 600 nm shell with degenerate planar anchoring at both confining interfaces, cross-polarized micrograph of 700 nm thick hybrid aligned shell with homeotropic anchoring at the outer interface, director field showing the stripe pattern in cholesteric shells with outer homeotropic surface anchoring, definition of skyrmion structures and snapshots showing the director field and defect points in skyrmions, reflection and transmission mode cross-polarized images of degenerate planar cholesteric and BPs shells with a thickness of 4 μm and various outer shell radius, Initial configurations for BPI and BPII shells obtained from the corresponding ansatz (PDF)

Movie: stripes pattern formation on a cholesteric high-chirality liquid crystal core–shell with a high degree of curvature and P(in)–H(out) surface anchoring. (MP4)

AUTHOR INFORMATION

Corresponding Authors

Monirosadat Sadati – *Department of Chemical Engineering, University of South Carolina, Columbia, South Carolina 29208, United States;* orcid.org/0000-0001-9701-9637; Email: sadati@cec.sc.edu

Juan J. de Pablo – *Pritzker School of Molecular Engineering, University of Chicago, Chicago, Illinois 60637, United States; Argonne National Laboratory, Lemont, Illinois 60439, United States;* orcid.org/0000-0002-3526-516X; Email: depablo@uchicago.edu

Jose A. Martinez-Gonzalez – *Facultad de Ciencias, Universidad Autónoma de San Luis Potosí, San Luis Potosí 78210 San Luis Potosi, México;* orcid.org/0000-0001-7257-8889; Email: jose.adrian.martinez@uaslp.mx

Authors

Sepideh Norouzi – *Department of Chemical Engineering, University of South Carolina, Columbia, South Carolina 29208, United States*

Antonio Tavera-Vazquez – *Pritzker School of Molecular Engineering, University of Chicago, Chicago, Illinois 60637, United States;* orcid.org/0000-0001-8304-2123

https://doi.org/10.1021/acsnano.2c02799
ACS Nano 2022, 16, 15894–15906

Johanan Ramirez-de Arellano − *Facultad de Ciencias, Universidad Autónoma de San Luis Potosí, San Luis Potosí 78210 San Luis Potosi, México*

Dae Seok Kim − *Department of Polymer Engineering, Pukyong National University, Busan 48513, South Korea;* orcid.org/0000-0002-7481-1434

Teresa Lopez-Leon − *Laboratoire Gulliver, UMR CNRS 7083, ESPCI Paris, Université PSL, 75005 Paris, France;* orcid.org/0000-0002-3272-6389

Complete contact information is available at: https://pubs.acs.org/10.1021/acsnano.2c02799

Author Contributions

S.N., J.A.M.-G., J.J.d.P., and M.S. conceived the work, and S.N. and A.T.-V. performed experiments. D.K. and T.L.-L. provided device fabrication support. J.A.M.-G. conceived and performed numerical simulations and theoretical calculations. J.R.d.A. helped with the simulations. S.N., T.L.-L., J.J.d.P., J.A.M.-G., and M.S. wrote the paper.

Notes

The authors declare no competing financial interest.

ACKNOWLEDGMENTS

This work has been supported by National Science Foundation, Division of Materials Research, Condensed Matter Physics program, with the NSF CAREER award 2146428. M.S. also acknowledges support provided by SC EPSCoR under grant 21-GE03. J.A.M.-G. acknowledges support from Ciencia de Frontera CONACYT grant CF-2019-74885 and computer resources, technical advice, and support provided by the Laboratorio Nacional de Supercómputo del Sureste de México (LNS), a member of the CONACYT national laboratories, with project 201901023N. J.J.d.P. was supported by the Department of Energy, Basic Energy Sciences, Division of Materials Science, under grant DESC0019762. The super-resolution confocal laser scanning microscopy technique was performed in the Integrated Light Microscopy Core at the University of Chicago, which receives financial support from the Cancer Center Support Grant (P30CA014599), RRID: SCR_019197.

REFERENCES

(1) Comerci, C. J.; Herrmann, J.; Yoon, J.; Jabbarpour, F.; Zhou, X.; Nomellini, J. F.; Smit, J.; Shapiro, L.; Wakatsuki, S.; Moerner, W. E. Topologically Guided Protein Crystallization Controls Bacterial Surface Layer Self-Assembly. *Nat. Commun.* **2019**, *10*, 2731.

(2) Wang, D.; Hermes, M.; Kotni, R.; Wu, Y.; Tasios, N.; Liu, Y.; de Nijs, B.; van der Wee, E. B.; Murray, C. B.; Dijkstra, M.; van Blaaderen, A. Interplay Between Spherical Confinement and Particle Shape on the Self-assembly of Rounded Cubes. *Nat. Commun.* **2018**, *9*, 2228.

(3) García, N. A.; Register, R. A.; Vega, D. A.; Gómez, L. R. Crystallization Dynamics on Curved Surfaces. *Phys. Rev. E* **2013**, *88*, No. 012306.

(4) Meng, G.; Paulose, J.; Nelson, D. R.; Manoharan, V. N. Elastic Instability of a Crystal Growing on a Curved Surface. *Science* **2014**, *343*, 634−637.

(5) Wang, D.; Dasgupta, T.; van der Wee, E. B.; Zanaga, D.; Altantzis, T.; Wu, Y.; Coli, G. M.; Murray, C. B.; Bals, S.; Dijkstra, M.; van Blaaderen, A. Binary Icosahedral Clusters of Hard Spheres in Spherical Confinement. *Nat. Phys.* **2021**, *17*, 128−134.

(6) De Gennes, P. G.; Jacques, P. *The Physics of Liquid Crystals*, 2nd ed.; Clarendon Press: Oxford, 1993; Vol. *23*.

(7) Kitzerow, H.-S.; Bahr, C.. *Chirality in Liquid Crystals*, 1st ed.; Springer: New York, 2001; pp 186− 218.

(8) Dubois-Violette, E.; Pansu, B. Frustration and Related Topology of Blue Phases. *Mol. Cryst. Liq. Cryst.* **1988**, *165*, 151−182.

(9) Wright, D. C.; Mermin, N. D. Crystalline Liquids: The Blue Phases. *Rev. Mod. Phys.* **1989**, *61*, 385.

(10) Oswald, P.; Pieranski, P. *Nematic and Cholesteric Liquid Crystals: Concepts and Physical Properties Illustrated by Experiments*, 1st ed.; CRC Press: Boca Raton, FL, 2005; pp 493− 547.

(11) Hu, W.; Wang, L.; Wang, M.; Zhong, T.; Wang, Q.; Zhang, L.; Chen, F.; Li, K.; Miao, Z.; Yang, D.; Yang, H. Ultrastable Liquid Crystalline Blue Phase from Molecular Synergistic Self-assembly. *Nat. Commun.* **2021**, *12*, 1440.

(12) Stegemeyer, H.; Blümel, T. H.; Hiltrop, K.; Onusseit, H.; Porsch, F. Thermodynamic, Structural and Morphological Studies on Liquid-crystalline Blue Phases. *Liq. Cryst.* **1986**, *1*, 3−28.

(13) Lin, T. H.; Li, Y.; Wang, C. T.; Jau, H. C.; Chen, C. W.; Li, C. C.; Bisoyi, H. K.; Bunning, T. J.; Li, Q. Red, Green and Blue Reflections Enabled in an Optically Tunable Self-organized 3D Cubic Nanostructured Thin Film. *Adv. Mater.* **2013**, *25*, 5050−5054.

(14) Popov, P.; Mann, E. K.; Jákli, A. Thermotropic Liquid Crystal Films for Biosensors and Beyond. *J. Mater. Chem. B* **2017**, *5*, 5061−5078.

(15) Guo, D. Y.; Chen, C. W.; Li, C. C.; Jau, H. H.; Lin, K. H.; Feng, T. M.; Wang, C. T.; Bunning, T. J.; Khoo, I. C.; Lin, T. H. Reconfiguration of Three-dimensional Liquid-crystalline Photonic Crystals by Electrostriction. *Nat. Mater.* **2020**, *19*, 94−101.

(16) Chen, C. W.; Hou, C. T.; Li, C. C.; Jau, H. C.; Wang, C. T.; Hong, C. L.; Guo, D. Y.; Wang, C. Y.; Chiang, S. P.; Bunning, T. J.; Khoo, I. C.; Lin, T. H. Large Three-dimensional Photonic Crystals Based on Monocrystalline Liquid Crystal Blue Phases. *Nat. Commun.* **2017**, *8*, 727.

(17) Całus, S.; Busch, M.; Kityk, A. V.; Piecek, W.; Huber, P. Chiral Phases of a Confined Cholesteric Liquid Crystal: Anchoring-dependent Helical and Smectic Self-assembly in Nanochannels. *J. Phys. Chem. C* **2016**, *120*, 11727−11738.

(18) Lin, P.; Wei, Z.; Yan, Q.; Chen, Y.; Wu, M.; Xie, J.; Zeng, M.; Wang, W.; Xu, J.; Cheng, Z. Blue Phase Liquid Crystal Microcapsules: Confined 3D Structure Inducing Fascinating Properties. *J. Mater. Chem. C* **2019**, *7*, 4822−4827.

(19) Lin, J. D.; Ho, Y.-L. D.; Chen, L.; Lopez-Garcia, M.; Jiang, S. A.; Taverne, M. P. C.; Lee, C. R.; Rarity, J. G. Microstructure-stabilized Blue Phase Liquid Crystals. *ACS Omega* **2018**, *3*, 15435−15441.

(20) Bukusoglu, E.; Wang, X.; Martinez-Gonzalez, J. A.; de Pablo, J. J.; Abbott, N. L. Stimuli-responsive Cubosomes Formed from Blue Phase Liquid Crystals. *Adv. Mater.* **2015**, *27*, 6892.

(21) Urbanski, M.; Reyes, C. G.; Noh, J.; Sharma, A.; Geng, Y.; Jampani, V. S. R.; Lagerwall, J. P. Liquid Crystals in Micron-scale Droplets, Shells and Fibers. *J. Phys.: Cond. Matt.* **2017**, *29*, 133003.

(22) Martínez-González, J. A.; Li, X.; Sadati, M.; Zhou, Y.; Zhang, R.; Nealey, P. F.; de Pablo, J. J. Directed Self-assembly of Liquid Crystalline Blue-phases into Ideal Single-crystals. *Nat. Commun.* **2017**, *8*, 15854.

(23) Seč, D.; Porenta, T.; Ravnik, M.; Žumer, S. Geometrical Frustration of Chiral Ordering in Cholesteric Droplets. *Soft Matter* **2012**, *8*, 11982.

(24) Enz, E.; Lagerwall, J. Electrospun Microfibres with Temperature Sensitive Iridescence from Encapsulated Cholesteric Liquid Crystal. *J. Mater. Chem.* **2010**, *20*, 6866.

(25) Guo, Y.; Afghah, S.; Xiang, J.; Lavrentovich, O. D.; Selinger, R. L.; Wei, Q. H. Cholesteric Liquid Crystals in Rectangular Microchannels: Skyrmions and Stripes. *Soft Matter* **2016**, *12*, 6312−6320.

(26) Orzechowski, K.; Sala-Tefelska, M. M.; Sierakowski, M. W.; Woliński, T. R.; Strzeżysz, O.; Kula, P. Optical Properties of Cubic Blue Phase Liquid Crystal in Photonic Microstructures. *Opt. Express* **2019**, *27*, 14270−14282.

(27) Tomar, V.; Hernandez, S. I.; Abbott, N. L.; Hernández-Ortiz, J. P.; De Pablo, J. J. Morphological Transitions in Liquid Crystal Nanodroplets. *Soft Matter* **2012**, *8*, 8679−8689.
(28) Fukuda, J. I.; Žumer, S. Ring Defects in a Strongly Confined Chiral Liquid Crystal. *Phys. Rev. let.* **2011**, *106*, No. 097801.
(29) Fukuda, J. I.; Žumer, S. Quasi-two-dimensional Skyrmion Lattices in a Chiral Nematic Liquid Crystal. *Nat. Commun.* **2011**, *2*, 246.
(30) Nych, A.; Fukuda, J. I.; Ognysta, U.; Žumer, S.; Muševič, I. Spontaneous Formation and Dynamics of Half-skyrmions in a Chiral Liquid-crystal Film. *Nat. Phys.* **2017**, *13*, 1215−1220.
(31) Fukuda, J. I.; Žumer, S. Novel Defect Structures in a Strongly Confined Liquid Crystalline Blue Phase. *Phys. Rev. lett.* **2010**, *104*, No. 017801.
(32) Yoshioka, J.; Ito, F.; Tabe, Y. Stability of a Double Twisted Structure in Spherical Cholesteric Droplets. *Soft Matter* **2016**, *12*, 2400−2407.
(33) Zhou, Y.; Bukusoglu, E.; Martínez-González, J. A.; Rahimi, M.; Roberts, T. F.; Zhang, R.; Wang, X.; Abbott, N. L.; De Pablo, J. J. Structural Transitions in Cholesteric Liquid Crystal Droplets. *ACS Nano* **2016**, *10*, 6484−6490.
(34) Posnjak, G.; Čopar, S.; Muševič, I. Points, Skyrmions and Torons in Chiral Nematic Droplets. *Sci. Rep.* **2016**, *6*, 26361.
(35) Darmon, A.; Benzaquen, M.; Seč, D.; Čopar, S.; Dauchot, O.; Lopez-Leon, T. Waltzing Route Toward Double-helix Formation in Cholesteric Shells. *Proc. Natl. Acad. Sci. U.S.A.* **2016**, *113*, 9469−9474.
(36) Tran, L.; Lavrentovich, M. O.; Durey, G.; Darmon, A.; Haase, M. F.; Li, N.; Lee, D.; Stebe, K. J.; Kamien, R. D.; Lopez-Leon, T. Change in Stripes for Cholesteric Shells via Anchoring in Moderation. *Phys. Rev. X.* **2017**, *7*, No. 041029.
(37) Durey, G.; Sohn, H. R.; Ackerman, P. J.; Brasselet, E.; Smalyukh, I. I.; Lopez-Leon, T. Topological Solitons, Cholesteric Fingers and Singular Defect Lines in Janus Liquid Crystal Shells. *Soft Matter* **2020**, *16*, 2669−2682.
(38) Lee, S. S.; Seo, H. J.; Kim, Y. H.; Kim, S. H. Structural Color Palettes of Core-shell Photonic Ink Capsules Containing Cholesteric Liquid Crystals. *Adv. Mater.* **2017**, *29*, 1606894.
(39) Geng, Y.; Jang, J. H.; Noh, K. G.; Noh, J.; Lagerwall, J. P.; Park, S. Y. Through the Spherical Looking-Glass: Asymmetry Enables Multicolored Internal Reflection in Cholesteric Liquid Crystal Shells. *Adv. Opt. Mater.* **2018**, *6*, 1700923.
(40) Tran, L.; Bishop, K. J. Swelling Cholesteric Liquid Crystal Shells to Direct the Assembly of Particles at the Interface. *ACS Nano* **2020**, *14*, 5459−5467.
(41) Martínez-González, J. A.; Zhou, Y.; Rahimi, M.; Bukusoglu, E.; Abbott, N. L.; De Pablo, J. J. Blue-phase Liquid Crystal Droplets. *Proc. Natl. Acad. Sci. U.S.A.* **2015**, *112*, 13195−13200.
(42) Palacio-Betancur, V.; Armas-Pérez, J. C.; Villada-Gil, S.; Abbott, N. L.; Hernández-Ortiz, J. P.; De Pablo, J. J. Cuboidal Liquid Crystal Phases Under Multiaxial Geometrical Frustration. *Soft Matter* **2020**, *16*, 870−880.
(43) Sadati, M.; Martinez-Gonzalez, J. A.; Zhou, Y.; Qazvini, N. T.; Kurtenbach, K.; Li, X.; Bukusoglu, E.; Zhang, R.; Abbott, N. L.; Hernandez-Ortiz, J. P.; de Pablo, J. J. Prolate, and Oblate Chiral Liquid Crystal Spheroids. *Sci. Adv.* **2020**, *6*, No. eaba6728.
(44) Sadati, M.; Martinez-Gonzalez, J. A.; Cohen, A.; Norouzi, S.; Guzmán, O.; De Pablo, J. J. Control of Monodomain Polymer-Stabilized Cuboidal Nanocrystals of Chiral Nematics by Confinement. *ACS Nano* **2021**, *15*, 15972−15981.
(45) Meister, R.; Halle, M.-A.; Dumoulin, H.; Pieranski, P. Structure of cholesteric focal conic domains at the free surface. *Phys. Rev. E* **1996**, *54*, 3771.
(46) Afghah, S.; Selinger, J. V. Theory of helicoids and skyrmions in confined cholesteric liquid crystals. *Phys. Rev. E* **2017**, *96*, No. 012708.
(47) Bogdanov, A. N.; Roßler, U. K.; Shestakov, A. A. Skyrmions is nematic liquid crystals. *Phys. Rev. E* **2003**, *67*, No. 016602.
(48) Utada, A. S.; Lorenceau, E.; Link, D. R.; Kaplan, P. D.; Stone, H. A.; Weitz, D. A. Monodisperse Double Emulsions Generated from a Microcapillary Device. *Science* **2005**, *308*, 537−541.
(49) Kim, S. H.; Park, J. G.; Choi, T. M.; Manoharan, V. N.; Weitz, D. A. Osmotic-pressure-controlled Concentration of Colloidal Particles in Thin-shelled Capsules. *Nat. Commun.* **2014**, *5*, 3068.
(50) Ravnik, M.; Žumer, S. Landau-de Gennes Modeling of Nematic Liquid Crystal Colloids. *Liq. Cryst.* **2009**, *36*, 1201−1214.
(51) Fournier, G.; Galatola, P. Modeling Planar Degenerate Wetting and Anchoring in Nematic Liquid Crystals. *Europhys. Lett.* **2005**, *72*, 403−409.
(52) Alexander, G. P.; Yeomans, J. M. Numerical Results for Blue Phases. *Liq. Cryst.* **2009**, *36*, 1215−1227.

https://doi.org/10.1021/acsnano.2c02799
ACS Nano 2022, 16, 15894−15906